Paramagnetic shimming for high-field MRI

D. Tomasi* and R.L. Wang
Medical Department, Brookhaven National Laboratory, Upton, NY 11973, USA.
(Received on 20 January, 2009)

The diamagnetism of biological tissues reduces the homogeneity of the magnetic field and may limit the number of samples in multi-sample gradient-recalled echo (GRE) experiments. This study aims to 1) evaluate the magnetic field distortions and signal loss artifacts in GRE images of proximal water samples, and 2) develop a passive shimming device to overcome this limitation. The magnetic field distribution produced by a diamagnetic H_2O sphere and a paramagnetic $CuSO_4$ disk in a secondary phantom were mapped using GRE experiments and the phase reference method, and compared to the corresponding magnetostatics models. The water sphere produced a pronounced signal loss artifact in amplitude images. This artifact was significantly reduced when the paramagnetic disk was placed symmetrically between the water sphere and the secondary spherical phantom. The present study suggests that the use of paramagnetic shimming devices can help to minimize susceptibility-related MRI signal losses and to increase the number of samples in multi-sample MRI experiments. The volume susceptibility and the shape of paramagnetic shimming devices could be optimized for particular setups and samples accordingly.

Keywords: susceptibility, passive shimming, signal loss

I. INTRODUCTION

The quality of magnetic resonance imaging (MRI) relies upon the presence of a highly homogeneous (and intense) magnetic field over the entire imaging sample. The homogeneity of the magnetic field is reduced by differences in magnetic susceptibility at air/tissue interfaces (1-3), which cause geometric distortion (2) and signal-loss artifacts (4) that are usually more pronounced for gradient-recalled echo (GRE) imaging modalities. These local field distortions can hardly be corrected by ordinary dynamic adjustment of electric currents in the active shimming coils of the MRI scanner largely due to the power limitations of the high-order shimming channels (5). Alternatively, magnetic materials can be used to correct local distortions of the static magnetic field, but the shape and size of the materials have to be customized for each particular sample (5). For instance, recent studies showed that a small amount of the strongly diamagnetic pyrolytic graphite placed underneath the roof of the mouth can significantly correct field inhomogeneities caused by the sinus cavity in the human orbitofrontal cortex (6,7).

Because diamagnetic biological tissues (4) alter the magnetic field in the surrounding space of the sample (2,3) and there is a growing interest for performing parallel image acquisition of multiple small-animals in clinical MRI scanners (8,9), it is important to evaluate the effect of between-sample proximity on image quality and to develop shimming methods to minimize the associated artifacts while maximizing the number of animals to be simultaneously scanned. Thus we aimed to evaluate the magnetic field distortions and the associated signal loss artifacts in GRE images of proximal water samples, and to develop a paramagnetic passive shimming device to correct these artifacts.

*Electronic address: tomasi@bnl.gov

METHODS

MRI acquisition

All studies were performed on a 4-Tesla Varian/Siemens MRI scanner using a fast low angle shot (10) pulse sequence (FLASH; 5 sagital slices; 4 mm thickness; 21 mm gap; in-plane resolution = 1.17×0.70 mm^2; acquisition matrix = 256×256; TR = 0.3 s; TE = 5 and 50 ms; phase encoding gradient step = 0.17 mT/m; slice selection gradient = 5.25 mT/m; readout gradient = 4.03 mT/m; acquisition bandwidth = 51.6 kHz; flip angle = 45^o).

All available active shimming channels (first and second order) were used to optimize the homogeneity of the magnetic field in the imaging volume. The constant field contours of the z-component of the magnetic field produced in the phantom volume by proximal diamagnetic or paramagnetic objects were measured using the phase reference method (11).

Paramagnetic shimming disk

A passive shimming disk was developed to minimize the extra magnetic field produced in the imaged phantom by the presence of the neighbor diamagnetic spherical phantom. A mix of 15-g of paramagnetic $CuSO_4$-$5H_2O$ salt crystal (Mallinckrodt Baker, Inc., Phillipsburg, NJ) and 32 g of Carpenter's wood glue (Elmer's Products, Inc., Columbus, HO) was deposited on a substrate (standard paper) and shaped as a disk with 4.25-cm outer diameter and 0.5-cm thickness. The disk was allowed to fully dry for 24 hours at room temperature. Finally, the paper substrate attached to the shimming disk was removed from it.

MRI Experiment

Four different images of a 13.5-cm outer-diameter spherical phantom filled with a 1mM $CuSO_4$ and 100 mM NaCl water solution were collected with the FLASH protocols for

each echo time: A) 16-cm apart (center-to-center), symmetrically placed with respect to the scanner isocenter, of an identical water phantom; B) same as A but with the paramagnetic disk at the scanner isocenter; C) with the paramagnetic disk at the scanner isocenter only; and D) the phantom alone as schematically shown in Fig. 1.

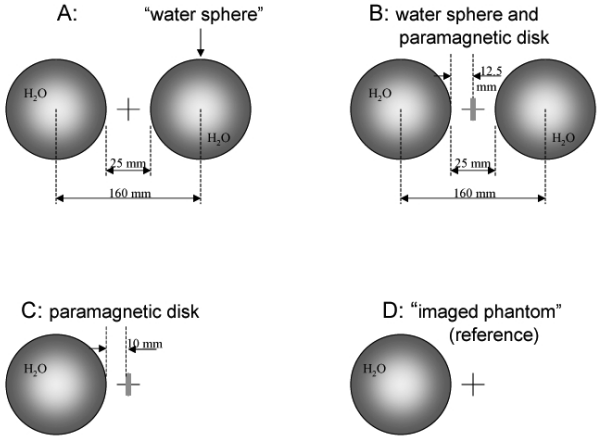

FIG. 1: Schematic representation of the four GRE experiments done with TE = 5, and 50 ms. A) Two identical spherical water phantoms ["imaged phantom" (left) and "water sphere" (right)] where symmetrically placed with respect to the scanner isocenter (cross). The "water sphere" reduces the field homogeneity in the "imaged phantom". B) The paramagnetic $CuSO_4$ disk is placed at the scanner isocenter between the "imaged phantom" and the "water sphere". The paramagnetic disk partially cancels out the field inhomogeneity produced by the water sphere in the "imaged phantom". C) The "imaged phantom" and the $CuSO_4$-disk remain in the scanner. The paramagnetic disk reduces the field homogeneity in the "imaged phantom". D) Only the left "imaged phantom" remains in the scanner for the reference image.

Phase reference imaging

In a GRE experiment the spins at $\mathbf{r} = (x, y, z)$ are partially refocused at the echo-time, TE, and accumulate a phase:

$$\phi(\mathbf{r}) = \gamma B_z(\mathbf{r})\, TE, \tag{1}$$

Here $B_z(\mathbf{r})$ is the offset of the static magnetic field at $\mathbf{r}$, and $\gamma = 267.522 \times 10^6$ rad/(sTesla) is the gyromagnetic ratio of protons. The complex MR signal at each imaging voxel can be written as

$$S(\mathbf{r}) = |S(\mathbf{r})| \exp(i\phi), \tag{2}$$

and the accumulated phase can be calculated as

$$\phi(\mathbf{r}) = tg^{-1}[S(\mathbf{r})]. \tag{3}$$

The magnetic field distribution produced by a magnetic object, P, in the vicinity of the imaging region can be calculated as the complex ratio of the MRI signals with, $S(\mathbf{r})^P$, and without , $S(r)^0$, the object (11)

$$\Delta\phi(\mathbf{r}) = tg^{-1}[S(\mathbf{r})^P / S(\mathbf{r})^0] = \gamma \Delta B_z(\mathbf{r}) TE \tag{4}$$

This phase reference measure of the phase of the voxel magnetization eliminates the spurious effects of B_O-field inhomogeneities (11,12), which are invariant across all conditions.

Fitting models

The magnetic volume susceptibilities of the diamagnetic water solution in the spherical phantom and the paramagnetic mix in the shimming disk were calculated using the theoretical expressions for the z-component of the magnetic field produced along the z-axis by a sphere and a disk with a uniform magnetization aligned with the external field B_0 (13):

$$\Delta B_z^{sphere}(0,0,z) = \frac{2\chi B_0 a^3}{3}\left(\frac{1}{z}\right)^3;$$
$$\Delta B_z^{disk}(0,0,z) = \frac{\chi B_0 R^2 l}{2}\left(\frac{1}{z}\right)^3. \tag{5}$$

Here χ is the magnetic susceptibility per unit volume, $B_0 = 4$ Tesla is the static magnetic field of the scanner, a is the radius of the spherical water phantom, and R and l are the radius and the thickness of the paramagnetic disk, respectively. A non-linear curve-fitting algorithm was used to calculate χ from axial measurements of $\Delta B_z(0,0,z)$ for the water sphere and the paramagnetic disk.

The z-component of the induced magnetic field gradient along the z-axis was calculated from field differences between adjacent voxels $G_z(0,0,z) = [\Delta B_z(0,0,z_i) - \Delta B_z(0,0,z_{i-1})]/(z_i - z_{i-1}))$.

A custom reconstruction program was written in IDL (Research Systems, Boulder, CO) to calculate the phase difference image, $\Delta\phi(\mathbf{r})$, and the distribution of the magnetic field and the magnetic field gradient from the ratio of two complex images, and to fit $\chi^{phantom}$ and χ^{disk} from the experimental magnetic field values using Eq. [5].

II. RESULTS

The separate experiments with the paramagnetic disk or the diamagnetic water sphere in the vicinity of the imaged phantom showed a pronounced signal loss artifact in the corresponding amplitude images (left Fig. 2, top and center panel, TE = 50-ms). However this artifact was significantly reduced in the experiment with both objects in the vicinity of the imaged phantom (left Fig. 2, bottom panel). The phase difference between the reference experiment (Fig. 1D) and experiments A and C (Fig. 1; TE = 5-ms) also showed the localized field inhomogeneity produced by either the phantom or the disk. The phase difference between experiments C and D demonstrates the partial cancellation of the field inhomogeneity produced separately by the diamagnetic phantom or the paramagnetic disk.

Fig. 3 (top panel) plots the amplitude of the MRI signal along the z-axis in the imaged phantom, relative to that in the reference experiment (D) at the same imaged voxels for experiments A, B, and C at TE = 50 ms. The diamagnetic water sphere produces a significant signal drop ($> 50\%$) within

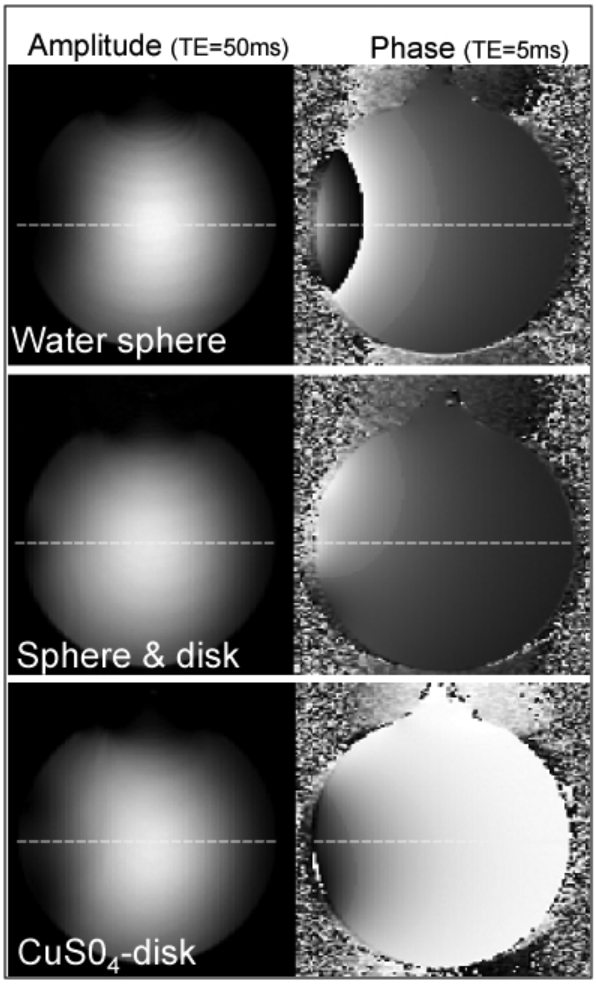

FIG. 2: Sagital views $(x = 0)$ of the MRI signal amplitude (left) and phase (right) in the "imaged phantom" for GRE experiments with long (50-ms) and short (5-ms) TE. The amplitude images with the paramagnetic $CuSO_4$ disk (bottom) or the diamagnetic H_2O sphere (top) show the signal loss (left) and phase wrapping (right) artifacts produced by the inhomogeneous magnetic field resulting from by these non-magnetic ($\chi << 1$) objects. The amplitude and phase images with the diamagnetic sphere and the paramagnetic disk show reduced artifacts (middle). The yellow dashed lines depict the z-axis.

an extended region near the phantom's edge (2.5 cm) due to intra-voxel spin dephasing. This artifact is significantly attenuated in the experiment with both objects (phantom and disk; 1B) because of their opposite magnetic properties. Figure 3 bottom shows that the magnetic field offset due to the water sphere in the imaged phantom was negative and decreased for closer distances, d, to the phantom wall. The magnetic field contribution of the disk, however, was positive, and the combined field contribution of the disk and the phantom varied slower with d. The maximum absolute magnetic field offset caused by the objects (A, B, and C) was lower than 8 mTesla. As shown in Fig. 4, the simple theoretical models in Eq. [5] explain the data with better precision than 95%. Note that the fitted susceptibility of the water solution in the phantom, $\chi(phantom) = -9.1 \pm 0.4 \times 10^{-6}$, matches that of the pure water(14)$\chi(H_2O) = -9.05 \times 10^{-6}$. The fitted susceptibility of the paramagnetic shimming disk was $\chi(disk) = 28 \pm 2 \times 10^{-6}$.

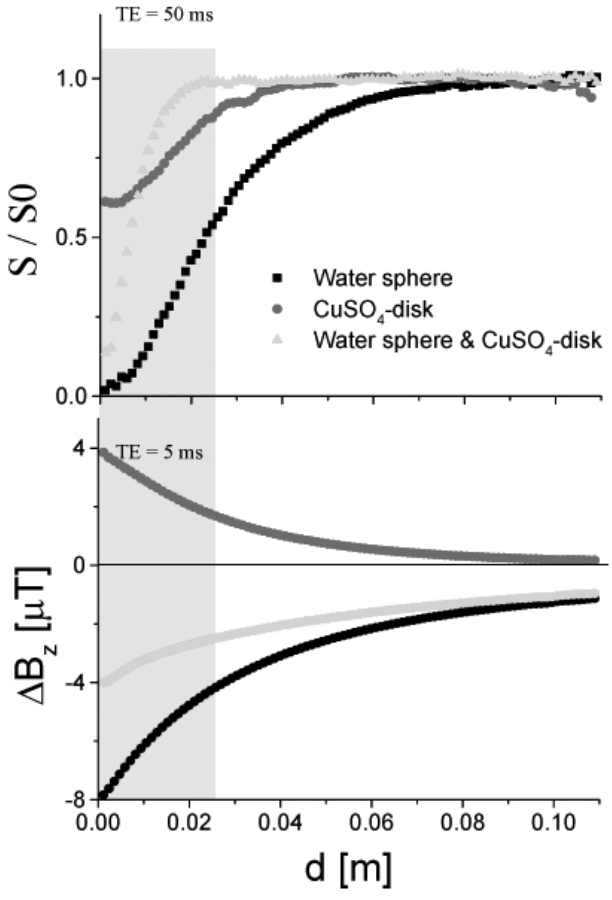

FIG. 3: Relative GRE signals for TE = 50-ms that quantify the signal-loss artifacts (top), and the induced magnetic field (bottom) as a function of distance, d, to the edge of the "imaged phantom" for all three experiments with non-magnetic objects (Figs. 1A-C).

Increased signal drop was associated to increased magnetic field offset and induced magnetic field gradients for all three different conditions (Fig.5). Note that for TE = 50-ms and the voxel size used in this study, higher induced magnetic field gradients than 0.175 mT/m caused near complete signal loss due to loss of coherence of spins within the voxel.

III. DISCUSSION

Here we showed that the induced magnetic field gradients resulting from the diamagnetism of a water sphere caused GRE-MRI signal losses larger than 50% for imaging voxels in the phantom that were closer than one radius to the nearby water sphere (Fig. 3 top). We further demonstrated that a paramagnetic shimming disk significantly corrects this signal loss artifact.

Multi-sample MRI with increasing number of samples requires closer proximity between samples, and the susceptibility-related signal loss artifacts may limit the number of samples in these experiments. As an example, a maximum of ten spherical water samples with 4-cm radius can be simultaneously imaged without signal losses larger than 50%

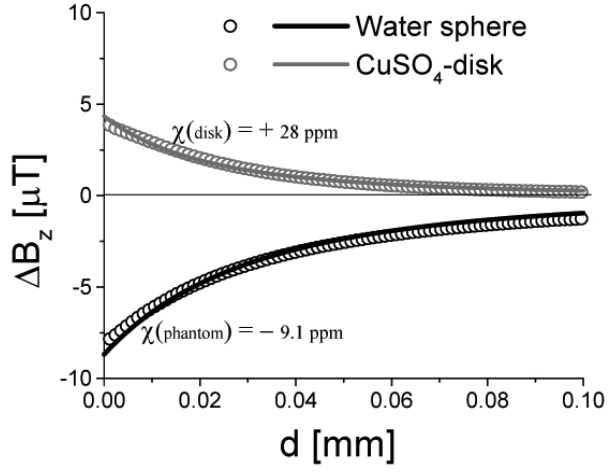

FIG. 4: Induced magnetic field produced by the water sphere and the $CuSO_4$-disk (symbols) as a function of distance, d, to the right edge of the "imaged phantom" and the corresponding fitting curves based in Eq. [5].

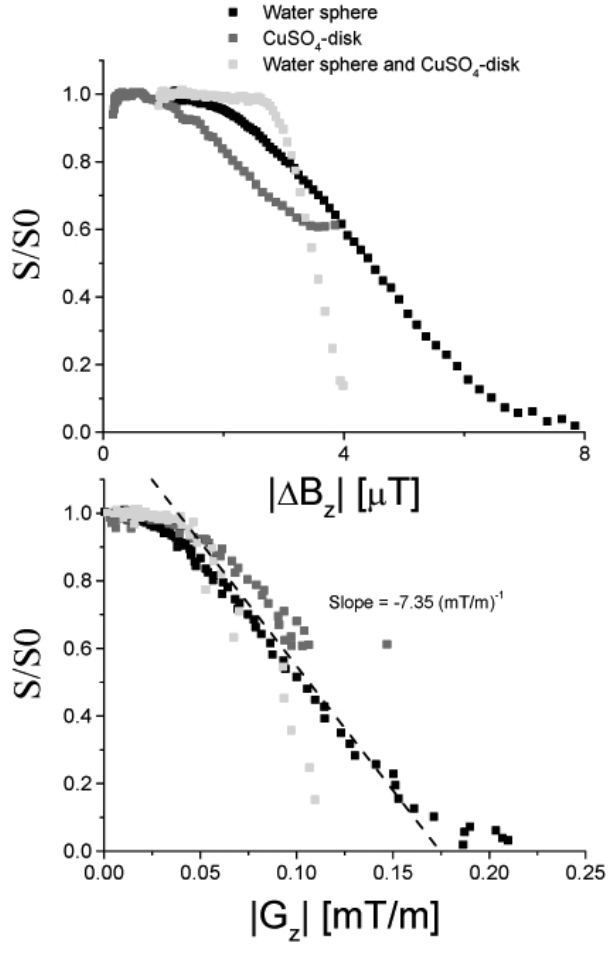

FIG. 5: Relative GRE signals for TE= 50-ms as a function of the amplitude of the induced magnetic field (top) or the induced magnetic field gradient (bottom) along the z-axis (Fig. 2; yellow dashed line) in the "imaged phantom" for all three experiments with non-magnetic objects (Figs. 1A-C).

in a 4 Tesla MRI scanner with a 32-cm diameter homogenous magnetic field volume (same pulse sequence parameters). This limitation would worsen with increased magnetic field strength.

The paramagnetic passive shimming disk significantly corrected the MRI signal loss artifact caused by the nearby water sphere (Figs. 2 and 3). Previous MRI studies in humans at 3 Tesla have placed diamagnetic pyrolytic graphite, which has a volume susceptibility $\chi_v = -4.00 \times 10^{-4}$ in one plane, underneath the roof of the mouth to reduce signal losses in the orbitofrontal cortex near the sinus cavity (6,7), and both bismuth, the most strongly diamagnetic material in nature ($\chi_v = -1.66 \times 10^{-4}$), and paramagnetic zirconium ($\chi_v = +0.92 \times 10^{-4}$) were used as passive shimming materials to homogenize the magnetic field in the mouse brain at 9.4 Tesla (5). The present study suggests that the use of paramagnetic shimming devices can help to minimize susceptibility-related MRI signal losses and to increase the number of samples in multi-sample MRI experiments. Bismuth and zirconium have stronger absolute magnetic susceptibility than our paramagnetic shimming disk ($\chi = +0.28 \times 10^{-4}$); therefore, smaller amounts of these passive shimming materials could be needed to shim the magnetic field. However, because bismuth and zirconium are metals they can perturb the homogeneity of the radio frequency field and affect the MRI signal-to-noise ratio as well as produce eddy current artifacts during MRI when they are close to the sample. Differently, our paramagnetic shimming disk does not produce signal loss or eddy current artifacts because it is not metallic. Our paramagnetic shimming disk was made using a mix of non-expensive available materials ($CuSO_4$ and carpenter glue) that can be easily shaped to shim arbitrary complex samples.

The magnetic field measurements in this work, which have a resolution of 1.5×10^{-8} Tesla (0.00375 ppm), are based on a variant of the phase reference imaging method (11,12) that depicts the constant magnetic field contours. In the present work and similarly to our previous study on macrovascular contributions in functional MRI studies (15), the differential phase accumulation between conditions was calculated from the complex ratio of two imaging experiments (Eq. [4]). These field measurements do not have contributions from B_0-inhomogeneities because the complex image ratio eliminates the common field contributions that are present in the two experiments.

In summary this study shows that for high-field gradient echo imaging, even weakly diamagnetic samples can distort the highly homogeneous field of the scanner enough to produce image artifacts in neighbor samples. The strength of the artifact is proportional to the induced magnetic field gradient in the neighbor samples. We developed a paramagnetic $CuSO_4$-passive shimming disk that reduces the induced magnetic field gradients and MRI signal losses by 80%.

[1] Truong T, Clymer B, Chakeres D, Schmalbrock P, Three-dimensional numerical simulations of susceptibility-induced magnetic field inhomogeneities in the human head Magn Reson Imaging 20 (2002) 759-770.
[2] Li S, Williams GD, Frisk TA, Arnold BW, Smith MB, A computer simulation of the static magnetic field distribution in the human head Magn Reson Med 34 (1995) 268-275.
[3] Li S, Dardzinski BJ, Collins CM, Yang QX, Smith MB, Three-dimensional mapping of the static magnetic field inside the human head Magn Reson Med 36 (1996) 705-714.
[4] Schenck J, The role of magnetic susceptibility in magnetic resonance imaging: MRI magnetic compatibility of the first and second kinds Med Phys 23 (1996) 815-850.
[5] Koch K, Brown P, Rothman D, de Graaf R, Sample-specific diamagnetic and paramagnetic passive shimming J Magn Reson 182 (2006) 66-74.
[6] Wilson J, Jenkinson M, Jezzard P, Optimization of static field homogeneity in human brain using diamagnetic passive shims Magn Reson Med 48 (2002) 906-914.
[7] Wilson J, Jenkinson M, Jezzard P, Protocol to determine the optimal intraoral passive shim for minimisation of susceptibility artifact in human inferior frontal cortex Neuroimage 19 (2003) 1802-1811.
[8] Bock N, Konyer N, Henkelman R, Multiple-mouse MRI Magn Reson Med 49 (2003) 158-167.
[9] Dazai J, Bock N, Nieman B, Davidson L, Henkelman R, Chen X, Multiple mouse biological loading and monitoring system for MRI Magn Reson Med 52 (2004) 709-715.
[10] Haase A, Frahm J, Hanicke W, Merboldt KD, FLASH imaging. Rapid NMR imaging using low flip angle pulses J Magn Reson 67 (1986) 257-266.
[11] Tomasi D, Panepucci H, Vidoto EL, Azevedo ER, Use of a phase reference for field mapping with amplitude images at low field J Magn Reson 131 (1998) 310–314.
[12] Tomasi D, Panepucci H, Magnetic field mapping with the phase reference method Magn Reson Imag 17 (1999) 157-160.
[13] Jackson JD. Classical Electrodynamics. New York: John Wiley and Sons; 1965.
[14] Schenck J, Safety of strong, static magnetic fields J Magn Res Imaging 12 (2000) 2-19.
[15] Tomasi D, Caparelli E, Macrovascular contribution in activation patterns of working memory J Cereb Blood Flow Metab 27 (2007) 33-42.